Improved Broadband Antenna Gain Measurements Through Multipath Mitigation Using Combined Robot Motion Stirring

Joshua A. Gordon, *Senior Member, IEEE*, and Benjamin L. Moser, *Member, IEEE*

***Abstract*—In this article we describe a technique developed at the National Institute of Standards and Technology (NIST) that uses coordinated motion of two robotic antenna positioners to mitigate the influence of chamber multipath reflections during antenna gain measurements. With this technique, through calibrated kinematic control of the robotic positioners, antenna-pair poses are dynamically changed relative to the bounds of the chamber while maintaining the measurement geometry in the reference frame of the antenna pairs. This creates a scenario where the chamber is effectively moving relative to the reference frame of the gain measurement geometry, thus resulting in "stirring" of the multipath chamber reflections. Through this stirring process, the effect of multipath reflections can be effectively averaged out, and antenna gain recovered even in the presence of appreciable multipath reflections. This technique is demonstrated with the three-antenna gain extrapolation method to improve gain calibrations that involve broadband dual-ridge horn antennas (DRHAs). Measurements were conducted in the WR430 and WR650 bands on NIST standard gain horn (SGH) reference antennas and lower gain broadband dual-ridge horn antennas using the NIST dual-robot Large Antenna Positioning System. Results show that antenna gain can be accurately determined with uncertainties of $\approx \pm 0.07$ dB, even when measurements are significantly perturbed by several dB due to chamber multipath reflections caused by the lower gain dual-DRHAs.**

***Index Terms*—Antenna gain, antenna, broadband, dual-ridge antenna, dual-ridge waveguide antenna, gain extrapolation, gain, multipath, reflections, robotic antenna measurements, wide band.**

I. Introduction

THE three-antenna gain extrapolation technique, as it is known today [1], [2], [3], [4], [5], [6], originated with the work of Paul F. Wacker at the National Bureau of Standards (NBS) [now the National Institute of Standards and Technology (NIST)] in the early 1970s and is considered to this day one of the most accurate techniques for obtaining antenna gain. The accuracy achieved by gain extrapolation can be attributed to the use of Wacker's signal expansion (1) representing the transmitted signal between two antennas

$$S_{ij}d = \sum_{p=0}^{\infty} \frac{e^{i(2p+1)kd}}{d^{2p}} \sum_{q=0}^{\infty} \frac{A_{pq}}{d^{q}} \quad . \tag{1}$$

Received 18 December 2025; revised 6 May 2026; accepted 12 June 2026. Date of publication 9 July 2026; date of current version 12 October 2026. *(Corresponding author: Joshua A. Gordon.)*

The authors are with the National Institute of Standards and Technology, Boulder, CO 80305 USA (e-mail: josh.gordon@nist.gov).

Digital Object Identifier 10.1109/TAP.2026.3709578

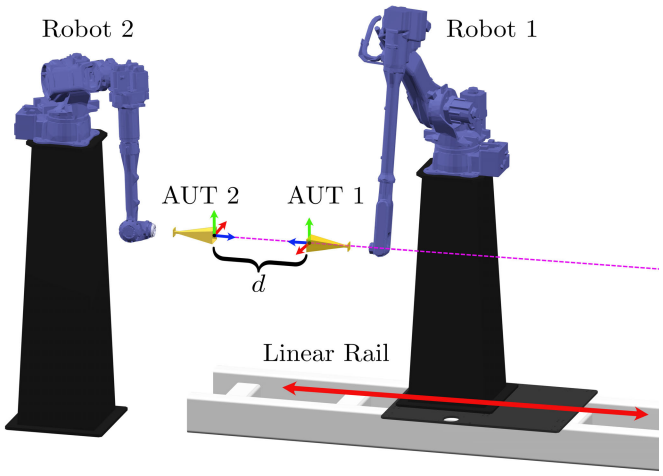


Fig. 1. LAPS diagram of general gain extrapolation setup showing the pair of antennas, $AUT1$ and $AUT2$ separated by distance, d. The linear rail direction of motion (red) defines the principle scan path aligned with the bore-sight axis of both antennas (magenta).

At any given antenna-to-antenna separation distance, d, the transmitted signal S_{ij} between antennas "i" and "j" accounts for all orders, p, of scattering, represented by the $e^{(2p+1)kd}$ terms, and orders, q, of proximity affects between antennas, represented by the A_{pq} coefficients. Here $k = 2\pi/\lambda$ and λ is the operating wavelength. Wacker's signal expansion is valid for antenna separation distances, from nearly touching to infinitely far away. Fig. 1 shows the gain extrapolation configuration for the 13-axis dual-robot Large Antenna Positioning System (LAPS) [7], [8], [9] at NIST Robotically Enhanced Antenna Laboratory for Metrology (REALM) [10]. As shown in the figure, scanning of the separation distance d between antennas under test (AUT), AUT1 and AUT2 is achieved using the two 6-axis robotic arms and the single-axis linear rail. Fig. 2 shows a photograph of a broadband dual-ridge horn antenna (DRHA) [11], [12] and WR430 standard gain horn (SGH) antenna mounted on the robotic arm positioners of the LAPS.

Through incorporating antenna-to-antenna scattering and proximity affects, gain extrapolation produces more accurate gain values than the three-antenna far-field technique, which assumes perfect far-field conditions at finite distances [13], [14]. For gain extrapolation, in practice, $S_{ij}d$ is measured for three pairs of antennas over a range of separation distances. The antenna gain term A_{00} (i.e., the lowest order term in (1)) is then found through post processing these data. The pair-gain

U.S. Government work not protected by U.S. copyright.

Authorized licensed use limited to: NIST Research Library & Museum. Downloaded on October 30,2026 at 14:24:13 UTC from IEEE Xplore. Restrictions apply.

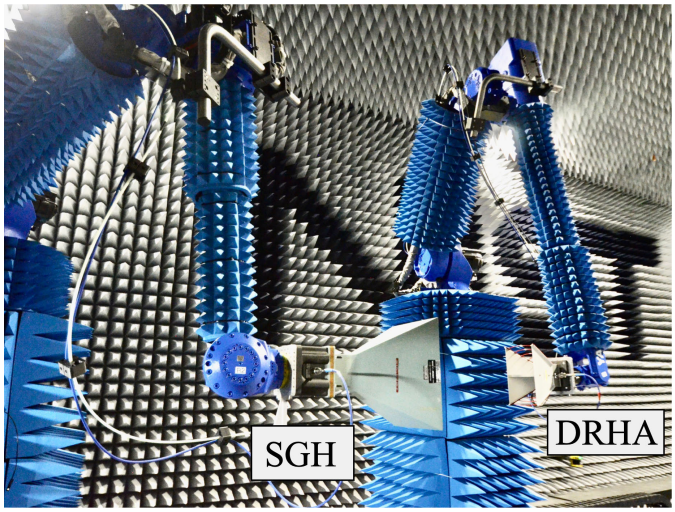


Fig. 2. Photograph showing the WR430 SGH and DRHA antennas mounted on the robotic arms of the NIST LAPS.

given as the product of the individual antenna gains g_i and g_j (in linear units) is then determined [3], [4] by

$$4k^2|A_{00}|^2 = g_i g_j. \tag{2}$$

A common post processing approach is via curve fitting the measured $|S_{ij}d|^2$ for three pairs of antennas and solving for $|A_{00}|^2$ and the antenna gains. As gain extrapolation is well documented, we refer the reader to [1], [2], [3], [4], and [5] for more details on its implementation.

Although Wacker's expression (1) is complete with respect to the dynamics of *direct antenna-to-antenna coupling*, it does not account for effects due to multipath reflections caused by residual reflections (echoes) in anechoic chambers or the testing environment [15], [16]. Depending on the antenna and chamber configuration, multipath reflections can be significant, causing perturbations in the measured transmission S_{ij} between antennas. As such, these perturbations will manifest as errors in the extrapolated gain values. Mitigating these multipath perturbations so as to render (1) effective for determining antenna gain in the presence of appreciable multipath reflections is the focus of this article and discussed in detail below.

Over the years, work has been developed to mitigate the errors in gain extrapolation due to multipath effects. More recently, filtering schemes based on either time domain [17], [18] and or spatial filtering [19] have been proposed to mitigate multipath reflections when performing gain extrapolation on omni-directional antennas, where large angle of arrival multipath echoes are dominant. These schemes rely on being able to resolve and differentiate the arrival of multipath reflection paths from the direct antenna-to-antenna signal through dense sampling in either time or spatial domains. These filtering schemes show promise for extremely wide beam omni-directional antennas where the direct signal path is quite separated in both space and time from the multipath reflection paths so that the direct signal can be effectively isolated. In practice, the filtering procedure must be tailored and tested for a particular set of antennas with varying results based on filter implementation. Furthermore, time domain filtering techniques are not amenable to narrowband antennas or single frequency operation as the frequency spectrum supported by the antenna operation must be wide enough to accommodate resolving multipath reflections. Spatial filtering techniques require accurate measurement of both phase and amplitude of the transmitted signal S_{ij} which becomes more challenging as long cable lengths in gain extrapolation systems act to distort phase information. As yet no guidelines exist on the design or implementation of these filters as related to the obtainable gain accuracy and associated levels of gain uncertainty.

In general, for directional and broad-beam type antennas such as SGH and DRHA, filtering techniques under gain extrapolation conditions are challenged to mitigate the strongest multipath reflections which arrive near coincident to the extrapolation axis and thus are most difficult to resolve and distinguish from the desired direct antenna-to-antenna signal of the antenna pairs. As such, it is beneficial to develop other techniques for mitigating multipath reflections that are more broadly applicable and which can be achieved through purely metrological implementations so that they provide a measure of convergence and uncertainty. As we will show below, leveraging the dynamic antenna positioning capability of modern robotic antenna ranges provides such a solution.

In this article, we present a metrology-based technique to mitigate multipath reflections in gain extrapolation measurements, thereby improving the accuracy of antenna gain. This technique leverages the unique capability of modern multirobotic antenna ranges to dynamically position pairs of antennas while maintaining antenna-to-antenna alignment. The technique is demonstrated using the NIST LAPS antenna range, where kinematic control of all 13-axes is used to dynamically and simultaneously move the antenna pairs so as to alter the gain extrapolation geometry within the chamber. This "stirring" of the antenna pair positions, effectively creates a distribution of multipath echoes for each antenna-to-antenna extrapolation scan separation distance d. The result being the multipath reflections can be effectively averaged out of the transmitted signal and the antenna gain accurately determined.

This technique does not require the use of specialized filtering techniques, nor is there a limitation on the frequency bandwidth of the antennas being measured, as it can be directly applied in single frequency operation. The knowledge of the transmitted signal phase is not needed, and this technique is amenable to directional and broad-beam antennas where multipath echoes may be close to coincident with the gain extrapolation measurement geometry.

Advantageously, this technique mitigates the strong multipath reflections produced by DRHAs. As will be shown below, this makes possible the use of broadband broad-beam DRHA for gain calibrations with accuracies as good as if SGH antennas alone were used. Being able to use DRHA in place of SGH antennas opens up the possibility to vastly improve their usability over their entire operational frequency range. The implications being significantly reduced setup and measurement time for broadband gain extrapolation calibrations, and reduced number of antennas when calibrating over broad frequency ranges.

II. Multipath Stirring Using 13-Axis Combined Robot Motion

Modern robotic antenna ranges [7], [8], [9], [20], [21], [22], [23], [24], [25], [26], [27], [28], [29], [30], [31], which are capable of manipulating the six degree of freedom (6 DoF) pose (position and orientation) of antennas,

Authorized licensed use limited to: NIST Research Library & Museum. Downloaded on October 30,2026 at 14:24:13 UTC from IEEE Xplore. Restrictions apply.

provide flexibility and configurability in antenna positioning and alignment. In the application of metrology for determining antenna parameters, such as pattern and on-axis gain, robotic antenna ranges have been successfully applied to near-field scanning and gain extrapolation. A unique capability of multirobotic antenna ranges is the ability to combine the motion ("combined robot motion") of multiple robots to simultaneously manipulate more than one antenna at a time. Here we implement combined robot motion to alter the gain extrapolation scan geometry relative to the reference frame of the antenna chamber, while maintaining the relative antenna-to-antenna alignment to effectively stir the multipath reflections during gain extrapolation measurements.

A. Inverse Kinematics and Dynamic Antenna Alignment

Under normal gain extrapolation conditions the AUT are aligned such that the origin and z-axis of their coordinate systems are coincident and maintained along the linear extrapolation scan path. While maintaining this alignment configuration, the antennas are separated along the scan path over a range of distances d, from the nearest distance d_{Near}, to the farthest distance d_{Far}. This is depicted in Fig. 1 and can be described as the transform, ${}^{1}\mathbf{T}_{2}$, between the coordinate systems (a.k.a "frames") AUT frame 1 to AUT frame 2. In the technique described here, to achieve effective stirring, the poses of each antenna in the pair are changed relative to the chamber coordinate system in such a way as to simultaneously maintain the relative alignment of each antenna needed for gain extrapolation. When executed correctly, the relative alignment of the coordinate systems of the individual antennas will move along the linear extrapolation path needed for the gain extrapolation measurement geometry while the entire gain extrapolation measurement geometry moves relative to the chamber coordinate system. This dynamic motion is achieved by solving the inverse kinematics that define the unified motion of the robotics and antenna coordinate systems so that the antenna poses can be controlled relative to all requisite coordinate systems simultaneously.

To minimize robot motion throughout the scan, the Z-axis of AUT 1 and AUT 2 are aligned to be coincident with the direction of motion of the linear rail of the LAPS and each other. The resultant relationship between the antenna frames is described as the homogeneous transformation matrix constructed from a translation of d of the Z axis and a rotation of π about the Y-axis as

$$ {}^{1}\mathbf{T}_{2} = \begin{bmatrix} -1 & 0 & 0 & 0 \\ 0 & 1 & 0 & 0 \\ 0 & 0 & -1 & d \\ 0 & 0 & 0 & 1 \end{bmatrix} \tag{3} $$

with expanded matrix form included for clarity. Provided a known lab coordinate system 0, aligned with the linear rail motion vector with known offsets to the robot base coordinate systems ${}^{0}\mathbf{T}_{R1,Base}$, the desired transform for the rail-mounted robot is initialized at an arbitrary feasible starting position aligned with the rail coordinate system as

$$ {}^{0}\mathbf{T}_{1} = \begin{bmatrix} \mathbf{I} & \boldsymbol{p}_{\text{start}} \\ \mathbf{0} & 1 \end{bmatrix}. \tag{4} $$

Then, the desired transform for Robot 2 can be solved as

$$ {}^{0}\mathbf{T}_{2} = {}^{0}\mathbf{T}_{1}\,{}^{1}\mathbf{T}_{2}. \tag{5} $$

The starting robot joint configurations to achieve these transforms $\boldsymbol{\theta}_1, \boldsymbol{\theta}_2$ are found by solving the inverse kinematics problem by using the native robot controller kinematics model or directly utilizing pose-error minimization as

$$ \arg\min_{\boldsymbol{\theta}} \quad \|\mathbf{E}(\boldsymbol{\theta}, \boldsymbol{\phi}, \mathbf{T}_{\text{des}})\| \tag{6} $$

where $\boldsymbol{\theta}$ is the joint configuration and $\boldsymbol{\phi}$ is the calibrated kinematic parameter set for a manipulator. For more in-depth discussion on inverse kinematics and their applications to multirobotic systems, such as the LAPS, the reader is referred to [32].

B. Multipath-Stirring Configuration

Upon solving the initial robot inverse kinematics for manipulating the poses of antenna pairs, the stirring configuration can be predefined and programmed. In this article, we present results for a stirring configuration that exercises three linear degrees of freedom and one rotation in the chamber coordinate system. The result being a manifold of diagonal linear extrapolation measurement paths contained within a cylindrical caustic surface within the chamber, each path displaced by a specified relative distance to the other. The choice of the extrapolation paths are informed by basic scattering principles such that the pointing of antennas normal to the walls of the chamber are avoided. By avoiding near-normal configurations multipath reflections are more effectively stirred over the extrapolation scan path.

The measurement locations, where the values of S_{ij} are recorded within the stirring configuration, are defined in the reference frame of the antenna pair just as would be done in a conventional gain extrapolation configuration. In defining the stirring locations, where the antennas are to be placed relative to the chamber, it is convenient to exploit the rectangular geometry of the anechoic chamber so that the chamber coordinate system is aligned with the chamber walls. Since the robot inverse kinematics have been solved for a priori (see Section II-A), each diagonal linear path is easily transformed and executed by the LAPS robots into cardinal coordinates along the orthogonal axes that are parallel to the chamber walls. Note, it is the *coordinates* which are parallel to the chamber walls yet the resulting antenna motion is along a diagonal path (i.e., nonnormal) relative to the chamber walls.

The nominal diagonal scan path at the center of the caustic was chosen based on the range of motion limits of the two robotic arms of LAPS. The longest wavelength and shortest wavelength in the operating band are denoted respectively as $\lambda_{\max}$ and $\lambda_{\min}$ with their ratio denoted as $\Lambda = \lambda_{\max}/\lambda_{\min}$. The stirring caustic, as decomposed along the orthogonal chamber coordinates, consisted of half-wavelength $\lambda_{\max}/2$ excursions in the positive and negative directions, for a total excursion of $\lambda_{\max}$ over each chamber coordinate and $\sqrt{3}\lambda_{\max}$ total excursion within the reference frame of the antenna pair. Individual stirring positions were separated by $\lambda_{\min}/10$ along each orthogonal chamber coordinate and $\sqrt{3}\lambda_{\min}/10$ in the reference frame of the antenna pair. The rotation θ was performed over the angular range of $\theta = [0°, 90°]$ for an angular excursion of $\Delta\theta = 90°$ at increments of $\delta\theta = 15°$. This resulted in a stirring manifold with a total of N gain extrapolation paths oriented diagonally within the LAPS chamber, each separated

Authorized licensed use limited to: NIST Research Library & Museum. Downloaded on October 30,2026 at 14:24:13 UTC from IEEE Xplore. Restrictions apply.

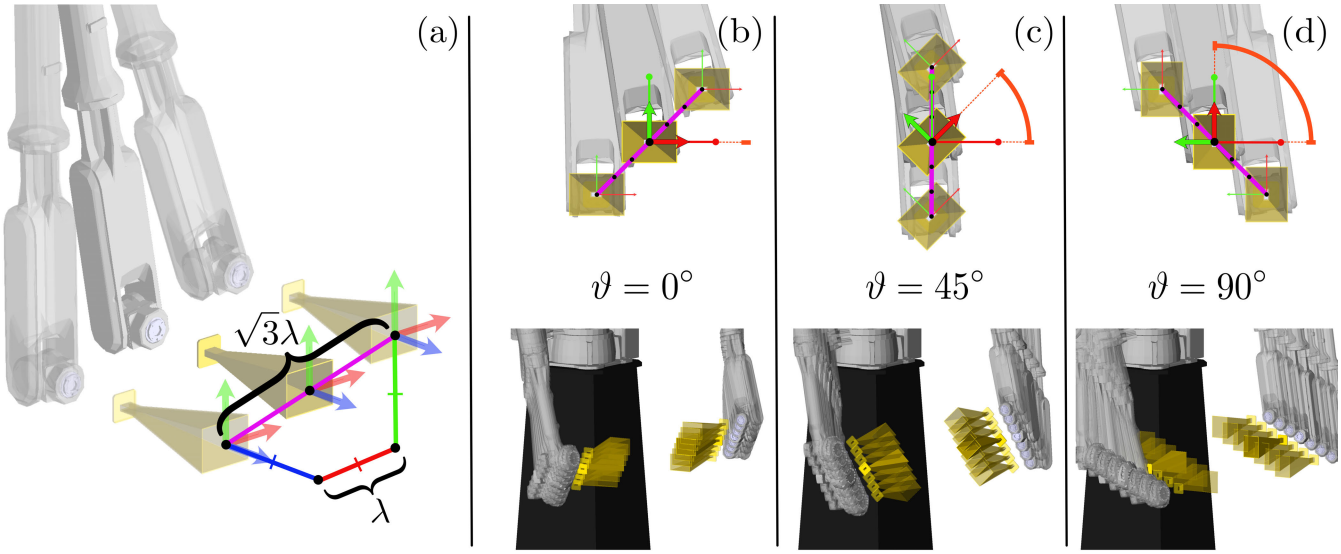


Fig. 3. LAPS stirring motion implementation. Stirring motion occurs on a centered diagonal with a traversal of $\lambda_{\max}$ in each cardinal direction relative to the laboratory coordinate system, resulting in a total motion of $\sqrt{3}\lambda_{\max}$ as shown in (a). The motion path is sampled at regular intervals, typically a fraction of the minimum wavelength, such as $\lambda_{\min}/10$. The antenna coordinate system is then rotated to angle ϑ with respect to the laboratory coordinate system and the diagonal sampling is repeated. Coordinate systems and resultant sample poses are illustrated at example locations in (b)–(d).

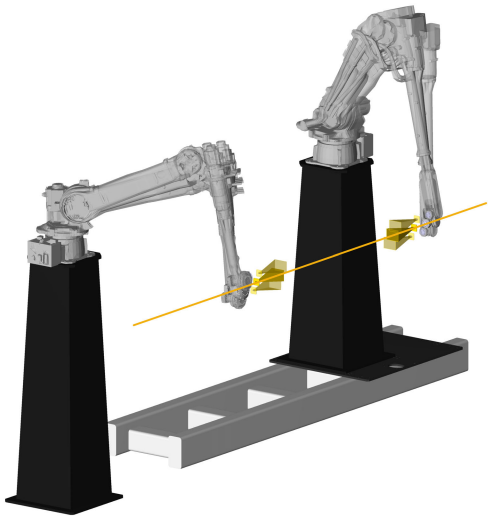


Fig. 4. Zoomed out perspective of the stirring motion of LAPS robots. The motion of the two robotic arms on LAPS motion is coordinated so that they move together to precisely and accurately maintain antenna-to-antenna alignment while the entire gain extrapolation path (yellow line) is moved within the chamber. Poses of the robot arms are depicted frozen at three stirring locations, while the yellow line depictss the robots maintaining the relative alignment and scan path of gain extrapolation between the antennas on each arm.

by $\sqrt{3}\lambda_{\min}/10$ in the reference frame of the antenna pair. The number of diagonal stirring paths N is given by

$$N = 10\Lambda\left(1 + \frac{\Delta\theta}{\delta\theta}\right). \tag{7}$$

This stirring configuration depicting the coordinate decomposition of the scan path robot motion is shown in Fig. 3 with Fig. 4 showing a zoomed out perspective.

Provided known transforms ${}^{0}\mathbf{T}_1$ and ${}^{0}\mathbf{T}_2$ between the lab frame and AUT frames that constitute the nominal extrapolation alignment, the stirring problem can be formulated as the application of a rotation about the Z axis R_z and a translation along a diagonal axis T_d. The resultant transforms are represented as

$${}^{0}\tilde{\mathbf{T}}_1 = {}^{0}\mathbf{T}_1 R_z(\vartheta)\, T_d\left(\mathbf{d}_j\right) \tag{8}$$

$${}^{0}\tilde{\mathbf{T}}_2 = {}^{0}\mathbf{T}_2 R_z(-\vartheta)\, T_d\left(-\mathbf{d}_j\right) \tag{9}$$

where opposite rotation values ϑ and position offsets $\mathbf{d}$ are required to preserve alignment between the AUT coordinate frames. At each stirring configuration at a particular rail location, the desired transform between the AUTs ${}^{1}\mathbf{T}_2$ is preserved.

III. Measurements

A. Measurement Setup

The measurement setup consisted of the LAPS antenna range outfitted with a 50 GHz vector network analyzer. The coordinate systems of the chamber, and antennas were defined through dimensional metrology of the antenna apertures using a laser tracking system. As an in-depth description of the LAPS and the use of laser trackers for robot-based antenna measurements is outside the scope of this article, the reader is refereed to [7], [8], [9], [20], [21], [29], and [30] for further details.

B. Antenna Configurations

Gain measurements using the stirring technique were performed on a set of five antennas. This set of antennas included two NIST reference SGH antennas of known gain values based on the conventional gain extrapolation technique, one in each of the WR650 (1.12–1.7 GHz) and WR430 (1.7–2.6 GHz) bands, and three broadband DRHA that operate over the frequency range of 1–18 GHz. The WR650 and WR430 bands were chosen as they cover frequencies where DRHA exhibit significant multipath effects and NIST reference antennas are available for measurement comparison. In addition, it is at frequencies where broadband DRHA provide advantages over

Authorized licensed use limited to: NIST Research Library & Museum. Downloaded on October 30,2026 at 14:24:13 UTC from IEEE Xplore. Restrictions apply.

SGH antennas such that the benefits of the stirring technique could make significant impact to the use of broadband DRHA. In particular, below 3 GHz SGH become increasing large and heavy compared to broadband DRHA, which remain compact and lightweight. Furthermore, below 3 GHz for a given span of frequencies, the number of frequency bands begins to significantly increases and correspondingly the number of SGH needed to cover a given span of frequencies increase while, a single broadband DRHA will cover the same span of frequencies. Other frequency bands are of interest and are a topic of future work.

This combination of antennas was chosen to demonstrate the effectiveness of the stirring technique to reduce the errors caused by multipath reflections resulting from broadband DRHA and thus: 1) enable broadband DRHA to be used to calibrated multiple single band SGH antennas with high accuracy and 2) enable high accuracy intrinsic calibration of broadband DRHA. The inclusion of the NIST reference antennas also provided a control set of antennas for an added level of validation of the measurement results beyond the self-consistency of the three-antenna method itself.

From these five antennas, three triplet sets were made. Two mixed triplets were made for the WR650 and WR430 bands using two DRHA and one SGH. One homogeneous triplet was made using the three DRHA. Measurements were performed at seven frequencies in the WR650 band and ten frequencies in the WR430 band where the SGH reference antennas have known gain values for a total of 17 frequencies. This included two measurements taken at the overlap frequency of 1.7 GHz between the WR430 and WR650 bands. Measurements on the homogeneous set of broadband DRHA were also performed at all 17 frequencies. From (7) the number of stirring paths for the antenna sets operating within either of the individual WR650 and WR430 bands is thus N = 105, and for the homogeneous DRHA set, which operates over both the WR650 and WR430 bands, N = 182 as Λ is larger.

IV. Analysis and Results

In this section we present the analysis and results for the stirring technique and the antenna gains obtained for all five antennas along with uncertainties. In addition, we discuss the convergence of this technique as it relates to the number of stirred extrapolation trajectories.

A. Static Coupling Curves

When implementing conventional gain extrapolation with a single, static, linear scan path, the coupling for a pair of antennas is given by the values of $|2kdS_{ij}|^2$ over the range of their separation distances. The coupling in decibels (dB) is given by $20log_{10}(|2kdS_{ij}|)$. In practice [3], the pair-gain is found from the lowest order of scattering (LOS) coupling, which from (1) can be written as

$$|2kdS_{ij}|^2 = g_i g_j + \frac{A'_{01}}{d} + \frac{A'_{02}}{d^2} + \frac{A'_{03}}{d^3} + \dots \tag{10}$$

with

$$A'_{01} = 4k^2\left(A_{00}A^*_{01} + A^*_{00}A_{01}\right)$$
$$A'_{02} = 4k^2\left(A_{00}A^*_{02} + A_{01}A^*_{01} + A^*_{00}A_{02}\right)$$
$$\vdots .$$

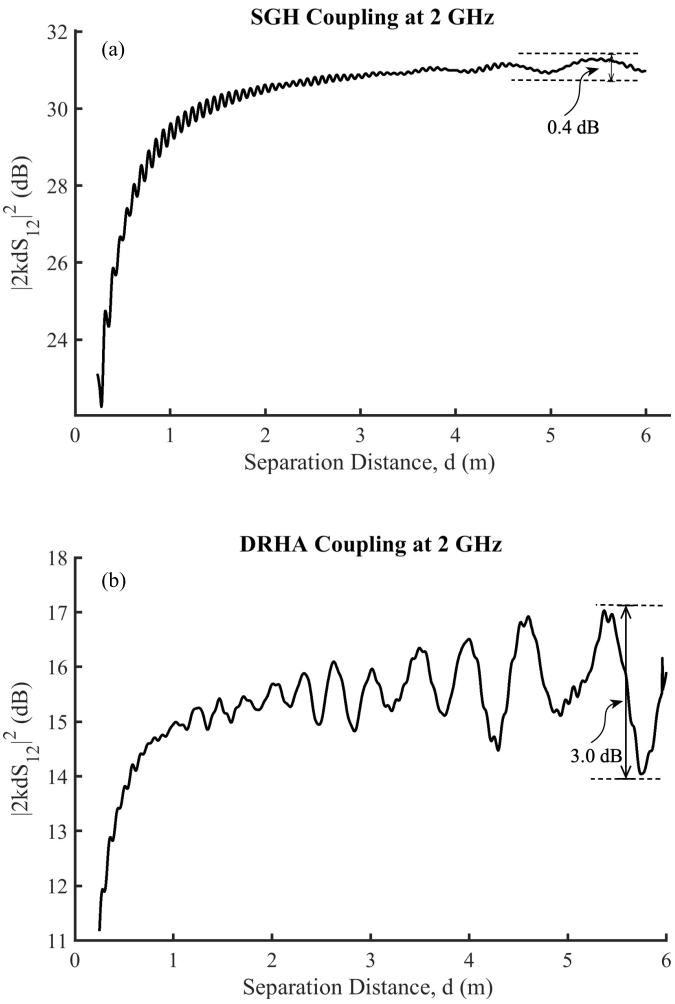


Fig. 5. Coupling curves at 2 GHz for (a) the WR430 SGHs and (b) the DRHAs. The long period oscillations in the plots arising from multipath reflections are stronger for the DRHA having a maximum peak-to-peak value of 3.0 dB compared to the SHG having a maximum peak-to-peak value of 0.4 dB.

The value of the LOS coupling curve approaches the pair-gain (in linear units) as d approaches infinity

$$\lim_{d\to\infty} |2kdS_{ij}|^2 = g_i g_j. \tag{11}$$

In observing the coupling, evidence of multipath reflections manifest as oscillations with periods larger than a wavelength [3], [16] and are distinguished from the fractional-wavelength oscillations that are due to the orders of mutual coupling scattering between antennas as described by (1). For a pair of directional antennas, the influence of multipath reflections on the coupling curve will have increasing influence as the separation distance is increased while the influence of mutual coupling will decrease [3]. Fig. 5 compares the influence of multipath scattering in the coupling curve for SGH and DRHA.

In Fig. 5(a) the coupling curve for a pair of 15 dB nominal gain, WR430 SGH antennas at 2 GHz is shown. In this figure the slower oscillations with period $\approx 6\lambda$ indicative of multipath effects become evident past d = 3 m. These multipath oscillations continue to grow to a peak-to-peak magnitude of $\approx$ 0.4 dB near the end of the 6.0 m extrapolation distance, whereas, the higher frequency mutual coupling oscillations diminish with increasing distance.

Authorized licensed use limited to: NIST Research Library & Museum. Downloaded on October 30,2026 at 14:24:13 UTC from IEEE Xplore. Restrictions apply.

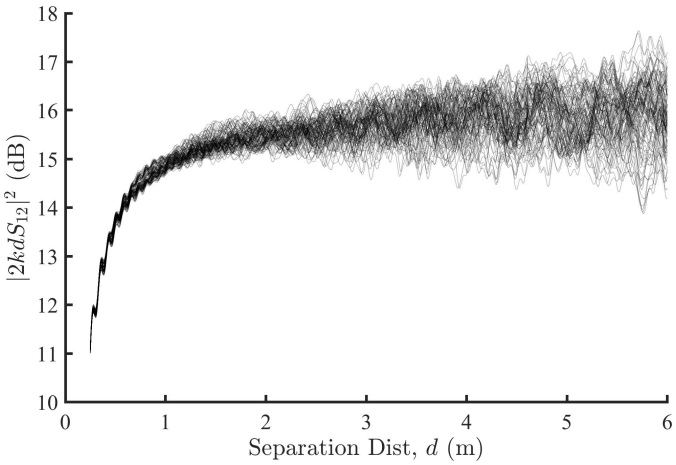


Fig. 6. Manifold of stirred coupling curves at 2 GHz for the pair of DRHAs.

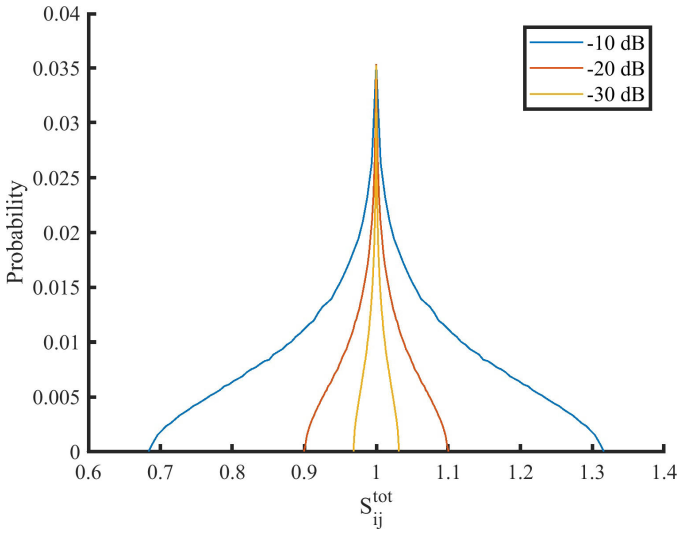


Fig. 7. Histogram plots of (12) for multipath values of −10, −20, and −30 dB.

In Fig. 5(b) the coupling curve for the pair of DRHA having a gain of ≈ 8.2 dB at 2 GHz is shown. Due to DRHA having lower gain (wider beams) more of the measurement chamber is illuminated at oblique angles causing a significant increase in the strength [33] and multitude of environmental multipath reflections. As such, DRHA show increased influence of multipath effects in the coupling curve compared to SGH, often over a wide range of separation distances, which become increasingly severe as distances increase. In the figure, the coupling curve is dominated by multipath reflections past $d = 1$ m having a period ≈ 3λ with the maximum peak-to-peak magnitude growing to ≈ 3.0 dB near the end of the 6.0 m extrapolation distance. Comparing the coupling curves in Fig. 5(a) and (b) for the SGH and DRHA respectively readily shows the increased effects of multipath for the DRHA. Where, for the SGH the maximum multipath perturbation is ≈ 0.4 dB and for the DRHA it is ≈ 3.0 dB.

As the coupling curve is directly related to the product of the antenna gains [see (11)], the distortion in the coupling curve caused by the multipath effects will result in errors in the gain values. As shown below in Section IV-B, the multipath effects depend on the extrapolation path chosen and thus the error in gain will also depend on which extrapolation path is used. However, as we also show below in Section IV-C, these errors can be mitigated through the stirring technique so that antenna gain can be determined with an accuracy as if the multipath distortions were insignificant.

B. Dynamic Stirred Coupling Curves

When executing gain extrapolation over the manifold of diagonal paths using the stirring technique (see Section II-B), a set of coupling curves is produced that represents the dynamic effects of multipath reflections. For each path in the manifold, the multipath reflection geometry between antennas and chamber boundaries changes, thus creating a distribution of multipath echoes. In the stirring configuration used here (see Section II-B), as the stirring paths change, the antennas are moved over a total distance of one-wavelength relative to the chamber coordinate system. Furthermore, with the use of the VNA, the signals arise from a single coherent source, thus multipath echoes are temporally coherent with respect to the antenna-to-antenna extrapolation signal. As such, at each antenna separation distance, the components of the multipath reflections have the opportunity to add in and out of phase. As a result of the manifold of changing stirring paths, and thus scattering geometry, a range of coupling values is produced at each separation distance d. An example of the coupling curves produced at 2 GHz that results from stirring the pair of DRHAs is shown in Fig. 6. As can be seen in the figure the stirring produces a distribution of coupling values at each separation distance.

C. Antenna Gain and Recovering the Coupling Curve

The interaction of multipath waves and the direct gain extrapolation coupling wave can be modeled as a two beam interference problem [15], [16]. The location of antennas i and j in the chamber coordinate system during stirring are described by vectors $\vec{r}_i$ and $\vec{r}_j$ with separation distance $d = |\vec{r}_i - \vec{r}_j|$. The direct coupling wave from (1) has complex amplitude $S(d)_{ij}$ and the multipath wave has complex amplitude $S(\vec{r}_i, \vec{r}_j)_{ij}^{mp}$ and relative phase$\phi_{mp}(\vec{r}_i, \vec{r}_j)$. The total wave observed is given by their superposition as

$$S\left(\vec{r}_i, \vec{r}_j\right)_{ij}^{tot} = S\left(d\right)_{ij} + S\left(\vec{r}_i, \vec{r}_j\right)_{ij}^{mp} e^{\phi_{mp}\left(\vec{r}_i, \vec{r}_j\right)}. \tag{12}$$

In an environment with a sufficiently large number of scattering paths, the multipath component of the total coupling signal will experience a wide range of phase and amplitude fluctuations so that on average the multipath effects will have zero mean. The act of stirring produces such an environment and through averaging the values of the measured signal at each distance d the LOS coupling in (10) can be recovered. Denoting the signal spatially averaged over all stirring paths as $\langle S(\vec{r}_i, \vec{r}_j)_{ij}^{tot} \rangle$ the resulting average signal is

$$\begin{aligned}\left\langle S\left(\vec{r}_i, \vec{r}_j\right)_{ij}^{tot} \right\rangle &= \left\langle S\left(d\right)_{ij} + S\left(\vec{r}_i, \vec{r}_j\right)_{ij}^{mp} e^{\phi_{mp}\left(\vec{r}_i, \vec{r}_j\right)} \right\rangle \\ &= S\left(d\right)_{ij}. \end{aligned} \tag{13}$$

Sincethe direct the antenna-to-antenna coupling $S(d)_{ij}$ is held at a constant distance d during stirring it is unaffected by the spatial average. As such the LOS coupling curve can be recovered from the averaged signal by

$$\left|2kd\left\langle S\left(\vec{r}_i, \vec{r}_j\right)_{ij}^{tot}\right\rangle\right|^2 = g_i g_j + \frac{A'_{01}}{d} + \frac{A'_{02}}{d^2} + \ldots. \tag{14}$$

Authorized licensed use limited to: NIST Research Library & Museum. Downloaded on October 30,2026 at 14:24:13 UTC from IEEE Xplore. Restrictions apply.

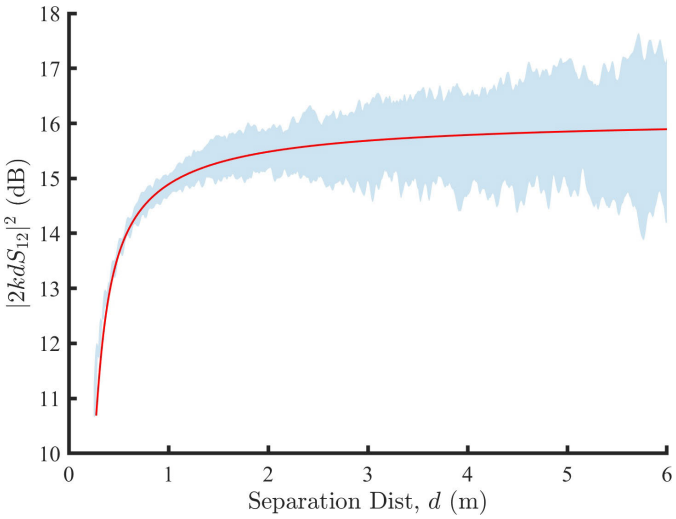


Fig. 8. Results of stirring and LOS curve recovery for the pair of DRHAs at 2 GH. Shown in light blue is the envelope of coupling values that result from the manifold of 105 stirring paths. The recovered LOS coupling curve is shown as the solid red curve.

This zero-mean behavior is also shown in the histograms in Fig. 7 where (12) is plotted for phases selected at random over $\phi = [0, 2\pi]$ for the case of $S(d)_{ij} = 1$ (i.e., 0 dB) and $S(\vec{r_i}, \vec{r_j})_{ij}^{mp}$ having values of -10, -20, and -30 dB. These values represent the physical scenario of attenuation of the absorbing material on the chamber walls reducing the multipath component amplitude relative to the direct signal. As can be seen in the figure the distributions are zero mean and centered on the direct coupling value of $S_{ij}^{tot} = S(d)_{ij} = 1$.

The pair-gains for each triplet is determined from the lowest order term that results from fitting the averaged data to the LOS curve in (14). An example of the recovery of the LOS coupling curve is shown in Fig. 8 for the pair of DRHAs at 2 GHz. In this figure the manifold of coupling curves produced by stirring is depicted by the light blue region along with the recovered LOS coupling curve shown as the solid red curve. The individual antenna gains are then calculated using the pair-gains in the conventional way via the three-antenna method [3]. With $\mathbb{G}_{ij} = 10log_{10}(g_i g_j)$ for each antenna pair ij, the gain for the individual antennas via the three-antenna method for the triplet are related by

$$\begin{bmatrix} G_1 \\ G_2 \\ G_3 \end{bmatrix} = \frac{1}{2} \begin{bmatrix} 1 & -1 & 1 \\ 1 & 1 & -1 \\ -1 & 1 & 1 \end{bmatrix} \begin{bmatrix} \mathbb{G}_{12} \\ \mathbb{G}_{23} \\ \mathbb{G}_{13} \end{bmatrix}. \tag{15}$$

D. Convergence of Gain Values

As the number of possible stirring paths can be numerous we provide an analysis to demonstrate the convergence of the gain values obtained using a finite and increasing number of stirring paths. As an example, in the case of a total of 105 stirring paths, there are up to 10^{30} possible n-choose-k combinations of stirring paths as shown by the blue curve in Fig. 9. As this is a prohibitively large number we limit the maximum number of combinations to 10^5 as shown by the red line in Fig. 9. The convergence of the gain values is observed as a function of the number of scan paths by randomly selecting a sample of k scan paths from the total of $N = 105$ paths and calculating the gains up to a maximum of 10^5 combinations. The results of this at 2 GHz for the mixed

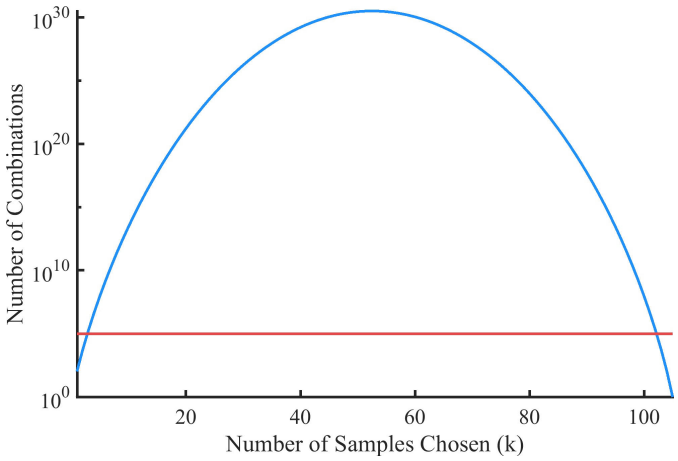


Fig. 9. Total number of n-choose-k possible extrapolation path combinations for the manifold of 105 stirred extrapolation paths (blue). The number of combinations reaches a very large peak, on the order of 10^{30}, around $k = 51$ extrapolation paths. A maximum of 10^5 combinations (red) are sampled to maintain computational feasibility.

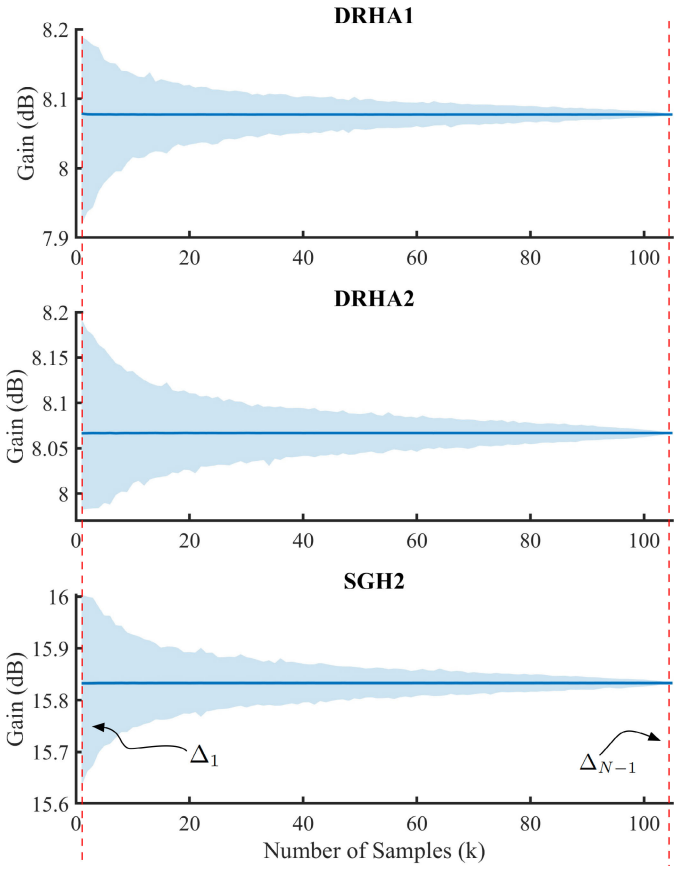


Fig. 10. Convergence of the value of antenna gain versus the number of stirred extrapolation paths sampled, k, out of a total of N, for the WR430 mixed pair of antennas at 2 GHz. The number of extrapolation paths sampled were chosen at random from all 105 paths in the stirring manifold. The light blue shaded region shows the range of values for the distribution of gain values at each value of, k. The resulting mean gain value is shown as the solid darker blue line. Δ_1 denotes the spread in gain values (when only regular gain extrapolation is used) for $k = 1$ giving 105 combinations, while Δ_{N-1} denotes the spread in gain values when $k = N - 1 = 104$ giving 105 combinations.

set {**DRHA1**, **DRHA2**, **SGH2**} are shown in the convergence plot in Fig. 10. In the figure the light blue shaded region in the convergence plot shows the spread in gain values and the

Authorized licensed use limited to: NIST Research Library & Museum. Downloaded on October 30,2026 at 14:24:13 UTC from IEEE Xplore. Restrictions apply.

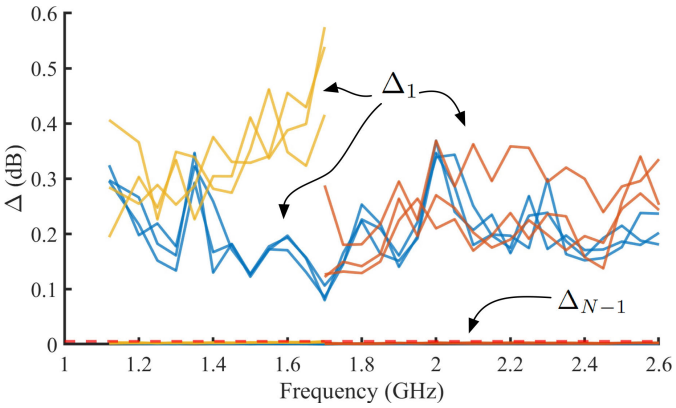


Fig. 11. Convergence parameters without stirring Δ_1 and with stirring Δ_{N-1}xs plotted for the gain convergence curves of the WR650 mixed set (Yellow), the WR430 mixed set (Orange), and the DRHA homogeneous set (Blue) at each frequency for each of the three antennas measured in each set. A significant reduction in the spread in gain values is observed when stirring is used, by up to two orders of magnitude, for all antenna at all frequencies with the spread in gain values bounded below $\Delta_{N-1} < 0.0056$ dB as indicated with the red dashed line.

solid blue curve shows the average of those gain values at a particular value of k.

In the figure, it is observed that the spread in gain values is reduced as the number of scan paths k used for stirring is increased. The error in gain values due to multipath effects without stirring, using only one path (i.e., regular gain extrapolation) is seen in the spread in values of the convergence plot at $k = 1$ and is denoted as Δ_1 in the figure. While the error in gain values due to the *residual* effects of multipath, left over after stirring, is seen in the spread in values of the convergence plot at $k = N - 1 = 104$ and denoted as Δ_{N-1} in the figure. Note, the number of combinations is 105 for both $k = 1$ and $k = 104$ however the number of stirring paths used has increased from 1 to 104.

Convergence analysis was performed for all antennas at all 17 frequencies with results comparing the gain error Δ_{N-1} (with stirring) and Δ_1 (without stirring) shown in Fig. 11. As can be seen in the figure, the gain error is significantly reduced from a maximum of $\Delta_1 \approx 0.55$ dB down to a residual multipath error with an upper bound of $\Delta_{N-1} \approx 0.0056$ dB shown by the red dotted line in the figure. Upon closer inspection, we observed that the spread in gain values as a function of the number of extrapolation paths used (as shown in the convergence plots of Fig. 10) follows directly the $1/N$ behavior expected of a normally distributed quantity, where $\Delta_{N-1}/\Delta_N = 0.0056/0.55 \approx 1/104 = 1/N$. As such, with intention, one may reduce the gain error due to multipath to a desired level by choosing the number stirring paths. To arrive at a (conservative) estimate for the gain error *due to multipath*, with and without stirring, these values are rounded up to the nearest whole digit giving, $\Delta_1 = 0.6$ dB and $\Delta_{N-1} = 0.01$ dB respectively. The resulting measurement uncertainty, inclusive of these gain errors, is discussed in Section IV-E.

E. Uncertainty Analysis

As a full exploration of uncertainty analysis is beyond the scope of this article, we provide an estimate for the expanded uncertainty comparing these measurements with and without stirring based on the well-established NIST uncertainty analysis for conventional gain extrapolation. An estimate of uncertainty, with and without stirring, is thus obtained by including Δ_1 and Δ_{N-1} respectively for the uncertainty contribution due to multipath effects in the overall uncertainty analysis. For the analysis the uncertainty contribution for multipath, u_{mp}, is taken as $u_{mp} = \Delta/2$, where Δ is taken as Δ_1 for the case without stirring, and Δ_{N-1} for the case with stirring. The resulting 95% expanded uncertainties [34], U, are given in Table I below where it is seen that without stirring $U = \pm 0.6$ dB and with stirring this has been reduced by about a factor of ten, to $U = \pm 0.07$ dB. As such, the resultant uncertainty is collapsed to the baseline uncertainty of < 0.1 dB expected of gain extrapolation in the absence of strong multipath effects thus demonstrating the stirring technique to affectively mitigate the effects of multipath.

TABLE I
GAIN UNCERTAINTY COMPARISON

	Standard Uncertainty (dB)	
Sources of Uncertainty	**Without Stirring**	**With Stirring**
Polarization Mismatch	$\ll 0.01$	$\ll 0.01$
RF System Variability	0.01	0.01
Impedance Mismatch	0.01	0.01
Antenna Alignment	0.01	0.01
Curve fit	0.02	0.02
Residual Multipath	***0.3***	***0.005***
Connector Repeatability	0.01	0.01
Random Uncertainties	0.02	0.02
(95%) Expanded Uncertainty, U (dB)	**0.60**	**0.07**

F. Gain Results

Results for the gain values using the stirring technique for the SGHs and the DRHA are shown in Table II and Table III respectively. In Table II the column labeled with **Ref** show the known values for the reference SGHs while the column labeled with **Meas** show the measured values obtained with the mixed antenna triplet {**DRHA1**, **DRHA2**, **SGH**}. In Table III the columns labeled with **Mixed** show the gain values of the DRHAs obtained with the mixed triplets and the remaining columns show the gain values of the DRHAs obtained with the homogeneous triplet of DRHAs, {**DRHA1**, **DRHA2**, **DRHA3**}. Beside each gain value in these tables are the expanded uncertainties, $\pm U$ from Table I.

Comparing gain values in Table II for the SGHs we see that the measured values agree with the reference values to within the uncertainties of the reference antennas. As such, this demonstrates the effectiveness of the stirring technique to accurately recover the SGH gain values in the presence of significant multipath caused by the lower gain and wider beam DRHAs. Furthermore, this also demonstrates that the stirring technique enables the use of broadband DRHAs *in place of SGHs* for conducting gain calibrations with the same high-level of accuracy as if SGHs alone were used.

Comparing the gain values for DRHA1 and DRHA2 in Table III for the mixed and homogeneous triplets also shows

Authorized licensed use limited to: NIST Research Library & Museum. Downloaded on October 30,2026 at 14:24:13 UTC from IEEE Xplore. Restrictions apply.

TABLE II
SGH GAIN RESULTS

Freq. (GHz)	SGH1 Meas	SGH1 Ref	SGH2 Meas	SGH2 Ref
1.12	14.40 ±0.07	14.39 ±0.07		
1.2	15.14 ±0.07	15.10 ±0.07		
1.3	15.74 ±0.07	15.79 ±0.07		
1.4	16.04 ±0.07	16.07 ±0.07		
1.5	16.51 ±0.07	16.51 ±0.07		
1.6	17.11 ±0.07	17.12 ±0.07		
1.7	17.06 ±0.07	17.06 ±0.07	14.05 ±0.07	14.02 ±0.07
1.8			14.75 ±0.07	14.79 ±0.07
1.9			15.53 ±0.07	15.55 ±0.07
2.0			15.80 ±0.07	15.82 ±0.07
2.1			15.93 ±0.07	15.99 ±0.07
2.2			16.33 ±0.07	16.34 ±0.07
2.3			16.64 ±0.07	16.65 ±0.07
2.4			16.98 ±0.07	16.91 ±0.07
2.5			17.08 ±0.07	17.11 ±0.07
2.6			16.96 ±0.07	16.88 ±0.07

TABLE III
DRHA GAIN RESULTS

Freq. (GHz)	DRHA1 Mixed	DRHA2 Mixed	DRHA1	DRHA2	DRHA3
1.12	7.68 ±0.07	7.61 ±0.07	7.72 ±0.07	7.70 ±0.07	7.75 ±0.07
1.2	7.40 ±0.07	7.30 ±0.07	7.41 ±0.07	7.40 ±0.07	7.51 ±0.07
1.3	7.48 ±0.07	7.46 ±0.07	7.45 ±0.07	7.54 ±0.07	8.44 ±0.07
1.4	7.99 ±0.07	7.98 ±0.07	7.99 ±0.07	8.06 ±0.07	9.11 ±0.07
1.5	8.61 ±0.07	8.51 ±0.07	8.60 ±0.07	8.58 ±0.07	9.10 ±0.07
1.6	9.12 ±0.07	9.05 ±0.07	9.11 ±0.07	9.11 ±0.07	8.90 ±0.07
(WR650) 1.7	9.67 ±0.07	9.57 ±0.07	9.67 ±0.07	9.65 ±0.07	8.89 ±0.07
(WR430) 1.7	9.68 ±0.07	9.61 ±0.07	9.67 ±0.07	9.65 ±0.07	8.89 ±0.07
1.8	10.09 ±0.07	10.08 ±0.07	10.08 ±0.07	10.11 ±0.07	9.16±0.07
1.9	9.74 ±0.07	9.81 ±0.07	9.75 ±0.07	9.85 ±0.07	9.20±0.07
2.0	8.21 ±0.07	8.18 ±0.07	8.16 ±0.07	8.14 ±0.07	8.50±0.07
2.1	8.14 ±0.07	8.01 ±0.07	8.14 ±0.07	8.06 ±0.07	8.73±0.07
2.2	9.49 ±0.07	9.39 ±0.07	9.46 ±0.07	9.43 ±0.07	9.07±0.07
2.3	10.11 ±0.07	10.12 ±0.07	10.09 ±0.07	10.13 ±0.07	8.77±0.07
2.4	10.54 ±0.07	10.45 ±0.07	10.48 ±0.07	10.50 ±0.07	8.80±0.07
2.5	10.63 ±0.07	10.60 ±0.07	10.66 ±0.07	10.65 ±0.07	8.93±0.07
2.6	10.38 ±0.07	10.40 ±0.07	10.37 ±0.07	10.44 ±0.07	9.15±0.07

agreement to within uncertainties. This demonstrates, in general, the effectiveness of the stirring technique for calibrating the gain of DRHA independent of including the higher gain SGH in the triplet. This is an important result as it opens the door for using DRHAs in place of SGHs for high accuracy broadband antenna calibrations. As such a single broadband DRHA could be used to cover many frequency bands whereas many SGH would be needed for an equivalent frequency range. Being able to use DRHAs alone significantly reduces the number of antennas needed for calibrations and size of antennas at lower frequencies and thus improves efficiency in calibration measurement work flows.

V. CONCLUSION

In this article we presented on a technique to effectively mitigate multipath reflections during gain extrapolation measurements. This technique demonstrates accurate gain calibrations for antennas that would otherwise prove challenging to measure, such as low gain broadband DRHAs. The technique leverages advantages of multirobotic antenna ranges to simultaneously manipulate pairs of antennas with respect to the anechoic measurement chamber so as to "stir" multipath reflections, thereby producing a zero-mean multipath environment. We show the gain error resulting from using N stirring paths can be reduced by a factor of $1/N$ and can thus be tractably reduced to insignificant levels even when multipath perturbations are significant. This technique was demonstrated using the NIST LAPS dual-robotic arm antenna range. Measurements were conducted over the WR650 and WR430 bands using sets of antennas comprised of NIST reference SGH antennas of known gain along with DRHAs. The DRHAs, being lower gain, exhibited significant multipath perturbation of the gain extrapolation coupling curve by as much as 3.0 dB. Results show a reduction of gain error from 0.55 dB down to 0.0056 dB when $N = 105$ and an overall reduction in the expanded gain uncertainty from ±0.6 dB *without* stirring to ±0.07 dB *with* the stirring technique. The stirring technique can thus enable a single broadband DRHA to be used as a low-uncertainty gain standard antenna during calibrations replacing multiple SGH antennas. The smaller size and weight of DRHAs compared to SGH antennas, especially at lower frequencies, furthers the benefits achieved through the stirring technique. These benefits significantly improve efficiency when performing gain calibrations and expand the operating range (frequency and gain) of antennas that can be measured, while maintaining low uncertainties commensurate with metrology-grade measurements. Traditionally, calibrations over the ten bands from 1 to 18 GHz performed using the three-antenna gain extrapolation method requires a set of 20 auxiliary antennas. Here, we show that using the stirring technique, *two* DRHAs can replace the entire set of twenty antennas, giving a tenfold improvement in calibration efficiency.

REFERENCES

[1] A. C. Newell and D. M. Kerns, "Determination of both polarisation and power gain of antennas by a generalised 3-antenna measurement method," *Electron. Lett.*, vol. 7, no. 3, pp. 68–70, Feb. 1971.

[2] A. Newell, R. Baird, and P. Wacker, "Accurate measurement of antenna gain and polarization at reduced distances by an extrapolation technique," *IEEE Trans. Antennas Propag.*, vol. AP-21, no. 4, pp. 418–431, Jul. 1973.

[3] A G. Repjar, A. C. Newell, and D. Tamura, "Extrapolation range measurements for determining antenna gain and polarization," *Nat. Inst. Standards and Technol.*, Gaithersburg, MD, USA, Tech. Rep. 1311, 1987.

[4] K. MacReynolds and M. Francis, "Antenna gain measurements the three-antenna extrapolation method," in *Proc. 21st Annu. Symp. Antenna Meas. Techn. Assoc. (AMTA)*, Nov. 1999, pp. 370–373.

[5] P. F. Wacker, "Theory and numerical techniques for accurate extrapolation of near-zone antenna and scattering measurements," *U.S. Department of Commerce*, Washington, DC, USA, NBS 10 733, Apr. 1972.

[6] *IEEE Recommended Practice for Antenna Measurements*, Standard 149–2021, 2022, doi: 10.1109/IEEESTD.2022.9714428.

[7] D. R. Novotny et al., "A multi-robot large antenna positioning system for over-the-air testing at the national institute of standards and technology," in *Proc. 39th Annu. Symp. Antenna Meas. Techn. Assoc. (AMTA)*, Oct. 2018, pp. 399–404.

Authorized licensed use limited to: NIST Research Library & Museum. Downloaded on October 30,2026 at 14:24:13 UTC from IEEE Xplore. Restrictions apply.

[8] D. R. Novotny, J. A. Gordon, M. S. Allman, J. R. Guerrieri, and A. E. Curtin, "Three antenna ranges based on articulated robotic arms at the National Institute of Standards and Technology: Usability for over-the-air and standard near-field measurements," in *Proc. IEEE Conf. Antenna Meas. Appl. (CAMA)*, Tsukuba, Japan, Dec. 2017, pp. 1–4, doi: 10.1109/CAMA.2017.8273367.
[9] J. Gordon and B. Moser, "NIST antenna gain and polarization calibration service reinstatement," in *Proc. Antenna Meas. Techn. Assoc. Symp. (AMTA)*, Renton, WA, USA, Oct. 2023, pp. 1–6, doi: 10.23919/amta58553.2023.10293530.
[10] Accessed: Jul. 6, 2026. [Online]. Available: https://www.nist.gov/ctl/robotically-enhanced-antenna-laboratory-metrology-realm
[11] J. Kerr, "Short axial length broad-band horns," *IEEE Trans. Antennas Propag.*, vol. AP-21, no. 5, pp. 710–714, Sep. 1973, doi: 10.1109/TAP.1973.1140561.
[12] J. L. Kerr, "Broadband horns," *Tech. Rep.* ECOM-3319, Aug. 1970.
[13] S. Schelkunoff and H. T. Friis, *Antenna Theory and Practice*. Hoboken, NJ, USA: Wiley, 1952.
[14] R. R. Bowman, "Field strength above 1 GHz: Measurement procedures for standard antennas," *Proc. IEEE*, vol. 55, no. 6, pp. 981–990, Jun. 1967, doi: 10.1109/PROC.1967.5712.
[15] J. Appel-Hansen, "Reflectivity level of radio anechoic chambers," *IEEE Trans. Antennas Propag.*, vol. AP-21, no. 4, pp. 490–498, Jul. 1973, doi: 10.1109/TAP.1973.1140524.
[16] B. Tian, "Free space VSWR method for Anechoic chamber electromagnetic evaluation," in *Proc. 30th Annu. Symp. Antenna Meas. Techn. Assoc. (AMTA)*, Nov. 2008, pp. 524–529.
[17] Z. Chen and Y. Wang, "Comparison of echo reduction techniques for omni-directional antenna calibration in an extrapolation range," in *Proc. 16th Eur. Conf. Antennas Propag. (EuCAP)*, Madrid, Spain, Mar. 2022, pp. 1–5, doi: 10.23919/EuCAP53622.2022.9768916.
[18] Z. Chen and Z. Xiong, "Differences of time domain gating implementions in vector network analyzers," in *Proc. Joint Int. Symp. Electromagn. Compat., Sapporo Asia–Pacific Int. Symp. Electromagn. Compat. (EMC Sapporo/APEMC)*, Sapporo, Japan, Jun. 2019, pp. 597–600, doi: 10.23919/EMCTokyo.2019.8893825.
[19] Z. Chen, Y. Wang, and D. Lewis, "Examination of antenna calibration methodologies in an extrapolation range," in *Proc. 16th Eur. Conf. Antennas Propag. (EuCAP)*, Madrid, Spain, Mar. 2022, pp. 1–4, doi: 10.23919/EuCAP53622.2022.9769087.
[20] J. A. Gordon, D. R. Novotny, J. R. Guerrieri, J. Coder, and M. Francis, "Robotically controlled mm-wave near-field pattern range," in *Proc. 34th Ant. Meas. Tech. Assoc. (AMTA)*, 2012, pp. 4086–4089.
[21] J. A. Gordon et al., "Millimeter-wave near-field measurements using coordinated robotics," *IEEE Trans. Antennas Propag.*, vol. 63, no. 12, pp. 5351–5362, Dec. 2015, doi: 10.1109/TAP.2015.2496110.
[22] J. A. Gordon, "Robotic antenna measurements," Eur. Assoc. Antennas Propag. (EuRAP), J. Rev. Electromagn. (RoE), Roadmap Paper, 2023, vol. 2, doi: 10.53792/RoE/2023/23003.
[23] M. Boroughs, "Robot room dual robots provide faster, more accurate antenna testing," *Innov. Quart. Boeing Corp.*, Dec. 2022, pp. 1–5.
[24] D. M. Lewis, J. Bommer, G. E. Hindman, and S. F. Gregson, "Traditional to modern antenna test environments: The impact of robotics and computational electromagnetic simulation on modern antenna measurements," in *Proc. 15th Eur. Conf. Antennas Propag. (EuCAP)*, Dusseldorf, Germany, Mar. 2021, pp. 1–5, doi: 10.23919/EuCAP51087.2021.9411068.
[25] D. J. van Rensburg, B. Walkenhorst, Q. Ton, and J. Demas, "A robotic near-field antenna test system relying on non-canonical transformation techniques," in *Proc. Antenna Meas. Techn. Assoc. Symp. (AMTA)*, Oct. 2019, pp. 1–5.
[26] J. Y. Kwon, C. Cho, and W. Chung, "Robot-based antenna measurement system for 6G frequency band," in *Proc. Korean Inst. Electromagn. Eng. Sci. (KIEES) Winter Conf.*, Feb. 2023, p. 1.
[27] P. A. Slater, J. M. Downey, M. T. Piasecki, and B. L. Schoenholz, "Portable laser guided robotic metrology system," in *Proc. Antenna Meas. Techn. Assoc. Symp. (AMTA)*, Oct. 2019, pp. 1–6.
[28] R. Moch and D. Heberling, "Fast spline-based antenna measurements for robotic test ranges via pointwise probe correction," in *Proc. 16th Eur. Conf. Antennas Propag. (EuCAP)*, Madrid, Spain, Mar. 2022, pp. 1–5, doi: 10.23919/EuCAP53622.2022.9769401.
[29] J. A. Gordon et al., "An all-metal, 3-D-printed CubeSat feed horn: An assessment of performance conducted at 118.7503 GHz using a robotic antenna range," *IEEE Antennas Propag. Mag.*, vol. 59, no. 2, pp. 96–102, Apr. 2017, doi: 10.1109/MAP.2017.2655574.
[30] B. Moser and J. Gordon, "Rapid automated antenna alignment on robotic antenna ranges," in *Proc. 18th Eur. Conf. Antennas Propag. (EuCAP)*, Glasgow, Scotland, 2024.
[31] B. L. Moser, J. A. Gordon, and A. J. Petruska, "Increased efficiency in planar near-field scanning using combined multi-robot motion," in *Proc. 19th Eur. Conf. Antennas Propag. (EuCAP)*, Stockholm, Sweden, Mar. 2025, pp. 1–5.
[32] B. L. Moser, J. A. Gordon, and A. J. Petruska, "Unified parameterization and calibration of serial, parallel, and hybrid manipulators," *Robotics*, vol. 10, no. 4, p. 124, 2021. [Online]. Available: https://doi.org/10.3390/robotics10040124
[33] V. Rodriguez, B. Walkenhorst, and J. Bruun, "Measurement of RF absorber at large angles of incidence using spectral domain transformations," in *Proc. Antenna Meas. Techn. Assoc. Symp. (AMTA)*, San Diego, CA, USA, Oct. 2019, pp. 1–6, doi: 10.23919/AMTAP.2019.8906360.
[34] B. N. Taylor and C. E. Kuyatt, "Guidelines for evaluating and expressing the uncertainty of NIST measurement results," Nat. Inst. Standards Technol., Gaithersburg, MD, USA, NIST Tech. 1297, 1994.



Joshua A. Gordon work has been published in book chapters and over 100 research papers for the advancement of antenna measurements and electromagnetic metrology. He is also an Inventor on several patents related to spatial metrology technologies with applications to antenna alignment and robot and robotic antenna range calibration as well as Rydberg atom based electric-field sensing.

Dr. Gordon is an Edmond S. Gillespie Fellow of the Antenna Measurement Techniques Association (AMTA). His work in robotics for use in mm-Wave antenna measurement applications was recognized by U.S. Department of Commerce, receiving the 2016 U.S. Department of Commerce Silver Medal for work on developing the Configurable Robotic Millimeter-Wave Antenna Range (CROMMA). His work in Rydberg atom-based sensors has also been highly recognized receiving the 2023 Department of Commerce Gold Medal and highest-honor Ron Brown Excellence in Innovation Award.



Benjamin L. Moser received the Ph.D. degree from Colorado School of Mines, Golden, CO, USA, in 2023.

After conducting research on the NIST robotic antenna ranges through the Professional Research Experience Program.

He is currently a Research Engineer at the Communications and Technology Laboratory, National Institute of Standards and Technology, Boulder, CO, USA. His research interests include robotic antenna metrology, inclusive of the design and control of parallel and hybrid robotic systems, supporting mechanisms, and processing software.

Authorized licensed use limited to: NIST Research Library & Museum. Downloaded on October 30,2026 at 14:24:13 UTC from IEEE Xplore. Restrictions apply.